

Research Article

Study on Fluid-Induced Vibration Power Harvesting of Square Columns under Different Attack Angles

Meng Zhang,¹ Guifeng Zhao,¹ and Junlei Wang²

¹School of Civil Engineering, Zhengzhou University, Zhengzhou 450001, China

²School of Chemical Engineering and Energy, Zhengzhou University, Zhengzhou 450001, China

Correspondence should be addressed to Junlei Wang; just4pipi@126.com

Received 4 April 2017; Revised 16 June 2017; Accepted 11 July 2017; Published 10 August 2017

Academic Editor: Micol Todesco

Copyright © 2017 Meng Zhang et al. This is an open access article distributed under the Creative Commons Attribution License, which permits unrestricted use, distribution, and reproduction in any medium, provided the original work is properly cited.

A model of the flow-vibration-electrical circuit multiphysical coupling system for solving square column vortex-induced vibration piezoelectric energy harvesting (VIVPEH) is proposed in this paper. The quasi steady state theory is adopted to describe the fluid solid coupling process of vortex-induced vibration based on the finite volume method coupled Gauss equation. The vibrational response and the quasi steady state form of the output voltage are solved by means of the matrix coefficient method and interactive computing. The results show that attack angles play an important role in the performance of square column VIVPEH, of which $\alpha = 45^\circ$ is a relatively ideal attack angle of square column VIVPEH.

1. Introduction

Recently, the development and utilization of new energy sources have become a research hotspot, among which the study of capturing energy from environment has received much more attention. One of the most important ways of environmental energy harvesting is capturing energy from fluid, which can be divided into two kinds, wind energy and water energy. Most of the traditional wind power and hydroelectric power facilities use the rotating turbine device to harvest energy with large volume device and low energy density. The micro energy technology, which can extract energy from environment and convert it into electric energy [1–4], has the features of functional continuity, small volume, and high energy density. In the late 1990s, the vibration piezoelectric energy harvesting technology has been widely used to harvest environmental flow energy and convert it into vibration energy [5–9], which is a kind of micro energy technology with continuous and nonconsuming energy supply. Therefore, it is an effective method for the microminiaturization of flow induced vibration energy harvesting device.

In fluid dynamics, there is a potential physical phenomenon that can be used for energy harvesting called

vortex-induced vibration. Vortex-induced vibration is that when the fluid flows through the bluff body, the formation and periodic shedding of the vortex will cause the vibration of the bluff body. Once the vibration intensity reaches a certain level, the flow field shedding will be locked, which results in large vibration energy. In other words, vortex-induced vibration is a kind of periodic, steady, or unsteady fluid structure interaction phenomenon, which has the characteristics of continuity and easy excitation [10, 11].

It is a challenging work to solve the problem of vortex-induced vibration energy harvesting. The key problem here is how to transform the flow energy into vibration energy efficiently. In recent years, many meaningful research works have been carried out on using vortex-induced vibration to collect ocean energy and wind energy. Among them, the energy conversion of circular bluff body piezoelectric vortex-induced vibration is mostly concerned. Allen and Smits [12] have studied the theory of energy harvesting of piezoelectric materials and designed an “eel” energy harvesting model which can be used to harvest the fluid kinetic energy in the water tank. On the basis of film theory, the “eel” model device can also be used to harvest the vortex shedding energy of “lock-in” phenomenon. Taylor et al. [13] used the “eel”

device of a PVDF polymer to harvest marine energy, which was placed in a water tank with the length of 241.3 mm, the width of 76.2 mm, and the thickness of 150 μm . The research shows that when the flapping frequency of PVDF closes to the vortex shedding frequency, the energy collection performance will be improved; the maximum voltage 3 V appears in the water flow velocity of 0.5 m/s. In Marine Renewable Energy Laboratory (MRELab) at the University of Michigan, Bernitsas et al. [14, 15] have presented a vortex-induced vibration for aquatic clean energy (VIVACE) to utilize the VIV phenomenon to generate power. The latter studies have been conducted in support of model tests for VIVACE converter, which harnesses hydrokinetic energy enhancing flow induced motions (FIM) and particularly VIV and various forms of galloping. Lee and Bernitsas [16, 17] built a device/system Vck to replace the physical damper/springs of the VIVACE with virtual elements. The testing was performed in the Low Turbulence Free Surface Water Channel of the University of Michigan at $40000 < \text{Re} < 120000$ and damping $0 < \xi < 0.16$. To continue and improve the work of VIVACE, which is used to convert hydrokinetic energy from ocean/river currents to electricity. Raghavan and Bernitsas [18, 19] conducted experiments in the regime right before transition from laminar to turbulent flow. Hysteresis was not observed in the experiments because the parameters remain in the 2P domain. Higher VIV amplitude of 2.1 to 2.7 diameters was obtained and the range of synchronization was increased by increasing the damping in VIVACE. Chang et al. [20] put a PTC device in the surface of the VIVACE converter to enhance the viscous damping; the results show that proper PTC could enhance the conversion efficiency of hydrokinetic energy to mechanical in VIVACE. For solving the problem of VIV, some excellent researches have also been conducted in MRELab. With the help of OpenFOAM software; Wu et al. [21] have developed a CFD code to solve the VIV problem of a single cylinder with PTC. Ding et al. [22] have also developed a CFD code in OpenFOAM to solve the VIV problem of multiple circular cylinders. Abdelkefi et al. [23, 24] and Mehmood et al. [25] investigated the possibility of harvesting energy from elastically mounted circular cylinders. They used, respectively, a wake oscillator model and direct numerical simulations to determine the fluctuating lift force. Abdelkefi et al. [23] reported that the aerodynamic nonlinearity results in the presence of hardening behavior. Both research studies determined the effects of the load resistance on the synchronization region and level of the harvested power. They demonstrated that maximum level of the harvested power can be associated with minimum values in the transverse displacement due to the shunt damping effect. To investigate the possibility of harvesting energy from other flow induced vibrations, different investigations have been performed. Abdelkefi and Nuhait [26] investigated the effects of cambered wing-based piezoaeroelastic energy harvesters on the flutter speed and the performance of the harvester. Dai et al. [27] and Yan and Abdelkefi [28] investigated the potential of harvesting energy from a combination of base excitations and VIV or galloping, respectively. Robbins et al. [29] proposed a device similar to the “eel” model, consisting of piezoelectric film arrays

(single size $203 \times 279 \times 0.5$ mm) with different configurations to collect wind energy generated by induced draft fan; the maximum output power is up to 10 mW. Akaydin et al. [30] proposed a structure (main size $30 \times 16 \times 0.2$ mm) which can separate the piezoelectric film from the bluff body, in which the maximum output power is $4 \mu\text{W}$. Gao et al. [31] carried out an experiment model (unit piezoelectric element size is 58×10 mm, cylinder diameter is 29.1 mm, and cylinder length is 36 mm), in which the cylinder is connected with the PZT cantilever beam, and the PZT beam is fixed at one end in the wind tunnel. Thus, electrical charges were accompanied by the wind-induced vibration of the PZT cantilever beam. The “lock-in” phenomenon is observed in the wind-induced vibration and a high voltage output is obtained in this region. Akaydin et al. [32] presented an energy harvesting experiment in a wind tunnel, in which the cylinder is connected with the free end of a cantilever beam with aluminum shim device. The results show that when the circuit resistance is changed, the natural frequency of the system will be changed also, so that the maximum value of the electromechanical coupling damping can be obtained. The above researches are mainly focused on the energy collection models of the cylindrical bluff body under vortex-induced vibration. Studies on the vortex-induced vibration and piezoelectric energy harvesting of noncylindrical section, such as square column and triangular column, are relatively less.

It is very important to consider the different attack angles in the analysis of square column vortex-induced vibration because of the asymmetry. The motion of the fluid at the edge of the square column is very irregular, which will greatly affect the vortex shedding near the column wall. The square column vortex shedding process is different from that of smooth circular cylinder; there is a direct vortex shedding without a smooth transition region. The boundary layer separation point of the square column is fixed at the corner of the leading edge without changing its position with the varying of Reynolds number. Therefore, it is of great practical significance to study on the influence of different attack angles of square column vortex-induced vibration piezoelectric energy harvesting (VIVPEH).

In this paper, a model of square column VIVPEH is presented, which can be used to investigate the mechanism of different attack angles on the energy capturing efficiency. The quasi steady state theory is adopted to describe the fluid solid coupling process of vortex-induced vibration based on the finite volume method coupled Gauss equation. Finally, the performance of different attack angles on the VIVPEH is carried out with considering the flow field parameters, the vibration characteristics, and the energy collection parameters.

2. Physical Model

The physical model of square column VIVPEH is shown in Figure 1, in which U stands for the inflow velocity, α stands for the angle between the square column and the inflow velocity, M is the mass of the column, K is the elastic coefficient of the

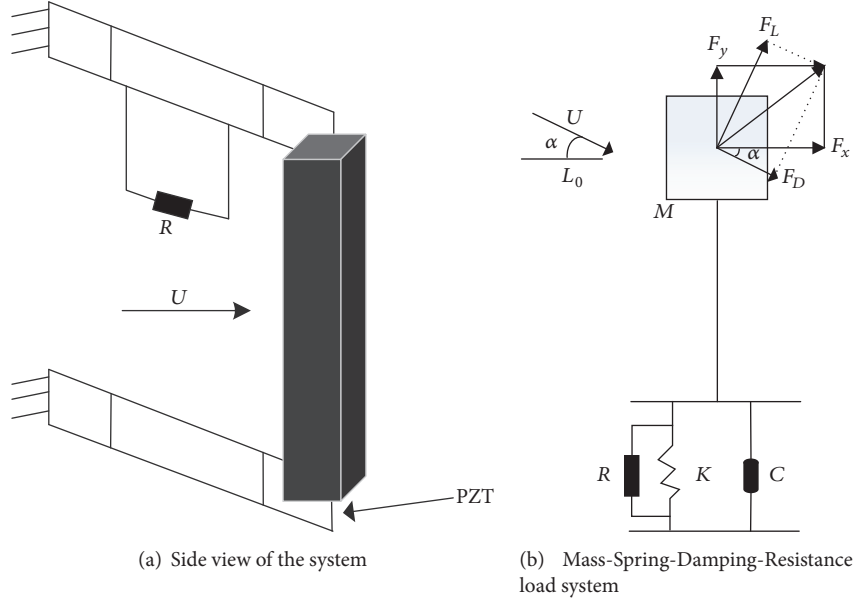


FIGURE 1: Physical model of square column energy harvesting system.

system, C is the damping of the system, and R is the external resistance load.

3. Mathematical Model of Energy Harvesting

To analyze the coupling process of three different fields, external flow field, vortex-induced vibration, and circuit, this paper uses the *Navier-Stokes* equation to describe the vortex-induced vibration, uses a linear second-order differential equation to describe the vortex-induced vibration of the single degree of freedom $M-C-K$ (mass spring damping) system, and finally uses coupled *Gauss law* and vibration equations to describe the electromechanical coupling system.

3.1. Fluid Solid Coupling Model. The external flow field is calculated by the continuity equation and the *Navier-Stokes* equation. Flow simulations presented in this paper are produced by open source CFD tool OpenFOAM, which is composed of C++ libraries solving continuum mechanics problems with a finite volume discretization method. Suppose the external flow field is 2D and unsteady. The time-dependent viscous flow solutions can be obtained by numerical approximation of the incompressible unsteady Reynolds-Averaged *Navier-Stokes* (URANS) equations in conjunction with the one-equation *Spalart-Allmaras* (S-A) turbulence model [33], where a second-order *Gauss* integration scheme with a linear interpolation is used in the governing equations for the divergence, gradient, and Laplacian terms. For time integration, second-order backwards *Euler* method is employed. The numerical discretization scheme has second-order accuracy in space and time. A pressure implicit with splitting of operators (PISO) algorithm is used for solving momentum and continuity equations together in a segregated way. The equations of motion for the square column are

solved using a second-order mixed implicit and explicit time integration scheme. The basic equations of URANS are

$$\begin{aligned} \frac{\partial U_i}{\partial x_i} &= 0, \\ \frac{\partial U_i}{\partial t} + U_j \frac{\partial U_i}{\partial x_j} &= -\frac{1}{\rho} \frac{\partial p}{\partial x_i} + \frac{\partial}{\partial x_j} \left(2\nu S_{ij} - \overline{u'_j u'_i} \right), \end{aligned} \quad (1)$$

where p is pressure, ρ is fluid density, ν is dynamic viscosity, U_i is the mean flow velocity vector, and S_{ij} is the strain rate tensor,

$$S_{ij} = \frac{1}{2} \left(\frac{\partial U_i}{\partial x_j} + \frac{\partial U_j}{\partial x_i} \right). \quad (2)$$

To solve the URANS equations for mean flow properties and potential turbulence flow, the Boussinesq eddy-viscosity approximation is adopted here, which relates to the Reynolds stress and the velocity gradient. The quantity $\overline{\rho u'_j u'_i}$ is the Reynolds stress tensor and can be modeled as $\overline{\rho u'_j u'_i} = 2\mu_t S_{ij}$, where μ_t is the turbulence eddy viscosity.

The S-A model is widely used for turbulence closure. The eddy-viscosity coefficient can be calculated from the following transport equation:

$$\begin{aligned} \frac{\partial \tilde{\nu}}{\partial t} + u_j \frac{\partial \tilde{\nu}}{\partial x_j} &= c_{b1} \tilde{S} \tilde{\nu} - c_{w1} f_w \left(\frac{\tilde{\nu}}{d} \right)^2 \\ &+ \frac{1}{\sigma} \left\{ \frac{\partial}{\partial x_j} \left[(\nu + \tilde{\nu}) \frac{\partial \tilde{\nu}}{\partial x_j} \right] \right\} + c_{b2} \frac{\partial \tilde{\nu}}{\partial \chi_i} \\ &\cdot \frac{\partial \tilde{\nu}}{\partial \chi_j}. \end{aligned} \quad (3)$$

In S-A model, the turbulence eddy viscosity μ_t can be obtained by

$$\mu_t = \rho \tilde{\nu} f_{v1}, \quad (4)$$

in which $f_{v1} = \chi^3 / (\chi^3 + c_{v1}^3)$, and $\chi \equiv \tilde{\nu} / \nu$, where χ is an intermediate value. $\tilde{\nu}$ is working variable of the turbulence model and depends on the transport equation (3).

The details of the transport equation are in Spalart and Allmaras [33], and the trip terms f_{t1} and f_{t2} are switched off and a ‘‘trip-less’’ initial condition was added for solving working variable $\tilde{\nu}$. This approach was successfully used in the work of Wu et al. [21] and Ding et al. [22] for circular cylinders.

The motion equations of a single degree of freedom M-C-K system can be represented by the following linear second-order differential equation:

$$M\ddot{Y} + C\dot{Y} + KY = F_y. \quad (5)$$

The relationships between M , K , and C are as follows:

$$\begin{aligned} \omega_n &= \sqrt{\frac{K}{M}}, \\ C &= 2\xi M\omega_n, \end{aligned} \quad (6)$$

where F_y stands for the force on unit volume of the flow field, which is perpendicular to the flow direction, Y stands for the column vibration displacement, \dot{Y} and \ddot{Y} represent the first- or second-order derivative of the column vibration displacement, respectively, ω_n is the natural circular frequency, and ξ is the dimensionless damping ratio. The dynamic response of the column can be obtained by solving the motion equations and the fluid governing equations simultaneously.

3.2. Electromechanical Coupling Model. In order to describe the relationship between the amplitude and the voltage in the vortex-induced vibration circuit, *Gauss law* is adopted in this paper. Theoretical derivations are as follows:

$$M\ddot{Y} + C\dot{Y} + KY - \theta V = F_y, \quad (7)$$

$$\theta\dot{Y} + C_p\dot{V} + \frac{V}{R} = 0, \quad (8)$$

where θ is the electromechanical coupling coefficient, C_p is the capacitance coefficient, and V is the voltage.

The influences of the vortex-induced vibration system on the circuit output voltage have been considered in (7) and (8), respectively. At the same time, the negative feedback effect of the circuit on the vibration system is also taken into account; that is to say, the influence of electromechanical coupling is considered. Combined with the flow field calculation results, we can carry out the flow-mechanical-electrical coupling analysis.

In order to solve the damping and natural frequency of the system, we use the matrix method to calculate the two-order nonhomogeneous ordinary differential equation (7). The homogeneous equation of (7) is as follows:

$$M\ddot{Y} + C\dot{Y} + KY - \theta V = 0. \quad (9)$$

Let $X_1 = Y$, $X_2 = \dot{Y}$, and $X_3 = V$; substitute (6) into (8) and (9); we can get

$$\begin{aligned} \dot{X}_1 &= X_2 \\ \dot{X}_2 &= -\omega_n^2 X_1 - 2\xi\omega_n X_2 + \frac{\theta}{M} X_3 \\ \dot{X}_3 &= -\frac{\theta}{C_p} X_2 - \frac{X_3}{RC_p}. \end{aligned} \quad (10)$$

The above equations can be expressed in the following matrix form:

$$\dot{X} = B(R) X, \quad (11)$$

where

$$X = [X_1, X_2, X_3]^T, \quad B(R) = \begin{bmatrix} 0 & 1 & 0 \\ -\omega_n^2 & -2\xi\omega_n & \frac{\theta}{M} \\ 0 & -\frac{\theta}{C_p} & -\frac{1}{RC_p} \end{bmatrix}. \quad (12)$$

The matrix $B(R)$ has three different eigenvalues of k_i , of which $i = 1, 2, 3$. Spalart and Allmaras [33] have pointed out that the first two eigenvalues are similar to the ones of vibration system without circuit, and yet the third eigenvalue is associated with the electromechanical coupling effect, such as piezoelectric system affected by the foundation or the aeroelastic excitation, and is negative constant. There are conjugate relations between k_1 and k_2 , in which the real part and the imaginary part of the conjugate solution stand for the damping and natural frequency of the electromechanical coupling system, respectively. Given that k_3 is negative constant, we consider only the real part of k_1 and k_2 , when computing the trivial solution of the matrix $B(R)$.

4. Quasi Steady State Model for Output Voltage

In this section, we adopt the quasi steady state model proposed by Barrero-Gil et al. [34] to describe the amplitude of vortex-induced vibration and calculate the time-varying vibration energy harvesting. When the vortex-induced vibration is in the synchronization region, the vibration amplitude of the system can be expressed as the following sine function:

$$Y = Y_{\max} \sin(\omega_n t), \quad (13)$$

where Y_{\max} is the maximum column vibration displacement.

It is worth noting that the voltage time-history curve and the vibration amplitude time-history curve are synchronous; that is to say, there is no phase difference. Substituting (13) into (11), we can get the analytical solution of the quasi steady state voltage with MATLAB.

$$\begin{aligned} V(t) &= \frac{\theta\omega_n R Y_{\max}}{1 + \omega_n^2 R^2 C_p^2} \left(e^{-t/RC_p} - \cos(\omega_n t) \right. \\ &\quad \left. - \omega_n R C_p \sin(\omega_n t) \right). \end{aligned} \quad (14)$$

TABLE 1: Calculation parameters for square column VIVPEH system.

Symbols and units	Physical meanings	Numerical values
M [kg]	Square column mass	0.2979
K [N/m]	Elastic coefficient of the system	579~584
C [N·s/m]	Damping of the system	0.0325~0.45
D_{squ} [m]	Square column side length	0.0016
α [degree]	Angle between the square column and the inflow velocity	0~75
ζ	Damping ratio of the system	0.00121
f_n [Hz]	Natural frequency of the system	7.012~7.132 (water)
C_p [nF]	Capacitance	120
θ	Electromechanical coupling coefficient	1.55×10^{-3}
μ [Pa·s]	Dynamic viscosity	0.0011379
ν [m ² /s]	Kinematic viscosity	1.139×10^{-6} (water)
ρ [kg/m ³]	Density	999.1026 (water)

The corresponding output power can be obtained by the following equation:

$$P(t) = \frac{V^2(t)}{R}. \quad (15)$$

The above mathematical expressions include the solving process of fluid solid coupling and electromechanical coupling.

First of all, we can get the flow field pressures P and F_y by solving the URANS equations in OpenFOAM. Secondly, we can obtain the column vibration displacement Y , the damping C , and natural circular frequency ω_n , by solving (5) to (11). It should be noted that the motion of the column is influenced by the pressure of the flow field. At the same time, the vibration of the column gives feedback to the flow field and causes the change of flow field distribution. Thus, the fluid solid coupling problem can be solved by interactive computing. Finally, the time-history curve of output voltage and output power can be obtained by (14) and (15). The above is the whole computing process of flow-vibration-electromechanical coupling system.

5. Numerical Results

5.1. Analysis Parameters and Cases. To carry out the numerical calculation of vortex-induced vibration, this paper provides the parameters of the vibration energy harvesting system, as shown in Table 1, in which D_{squ} is the side length of the square column, D_{Nor} stands for the dimensionless characteristic length of the square column, and the relationship between D_{Nor} and D_{squ} is given in

$$D_{\text{Nor}} = D_{\text{squ}} (\sin \alpha + \cos \alpha). \quad (16)$$

Based on the parameters of Table 1 and formula (16), we can calculate the numerical values of D_{Nor} as 0.0016 under 0° attack angle, 0.00196 under 15° attack angle, 0.00219 under 30° attack angle, 0.00226 under 45° attack angle, 0.00219 under 60° attack angle, and 0.00196 under 75° attack angle.

The computational grid and boundary conditions of square column vortex-induced vibration under different

attack angles are given in Figure 2, where the computational domain is $20 \times 20D$, and the entire domain includes five boundaries: velocity inlet, velocity outlet, top, bottom, and a column wall. The inlet velocity is considered as uniform and constant velocity. For outlet boundary, a zero gradient condition is specified for velocity. The top and bottom condition are defined as a wall boundary. In present numerical study, a moving wall boundary condition is applied for the square column when the column is in VIV. The two-dimensional, structured grids were generated with the help of ‘‘Gambit’’ software. The grid domain size is $20 \times 20D$. The square column was set in the center in the domain to ensure that the results of the numerical model are accurate. The conditions at the outlet are close to the assumed conditions. The computational domain in the vicinity of each cylinder is a $3 \times 3D$ square where the grid density for the near-wall region is enhanced to solve for high resolution in flow properties.

When the external resistance value is $R = 1 \times 10^6 \Omega$, the spring stiffness value of the square column VIVPEH system is $K_{\text{squ}} = 580 \text{ N/m}$, and the corresponding damping value is $C_{\text{squ}} = 0.2 \text{ Ns/m}$. Taking the range values of the flow velocity as 0.03927 m/s to 0.08975 m/s, we can calculate the numerical values of $U_{r\text{squ}}$ under different attack angles, as shown in Table 2, in which $U_{r\text{squ}}$ is the reduction velocity, defined as follows:

$$U_{r\text{squ}} = \frac{U}{f_n D_{\text{squ}}}, \quad (17)$$

where $f_n = \omega_n / 2\pi$.

In this paper, the matrix method is used to evaluate the influence of the external resistance load on the damping and natural frequency of the electromechanical coupling system by MATLAB. Then, the damping and natural frequency values can be used for initial conditions in OpenFOAM to compute the vibration amplitude of the vortex-induced vibration system under different Reynolds numbers ($94 < R_e < 115$). The main focus of this paper is to investigate the influence of external resistance load ($R = 1 \times 10^3 \Omega, 1 \times 10^4 \Omega, 1 \times 10^5 \Omega, 1 \times 10^6 \Omega, 1 \times 10^7 \Omega$) on the energy conversion of the square column VIVPEH system, including the effect on vibration amplitude, output voltage, and power.

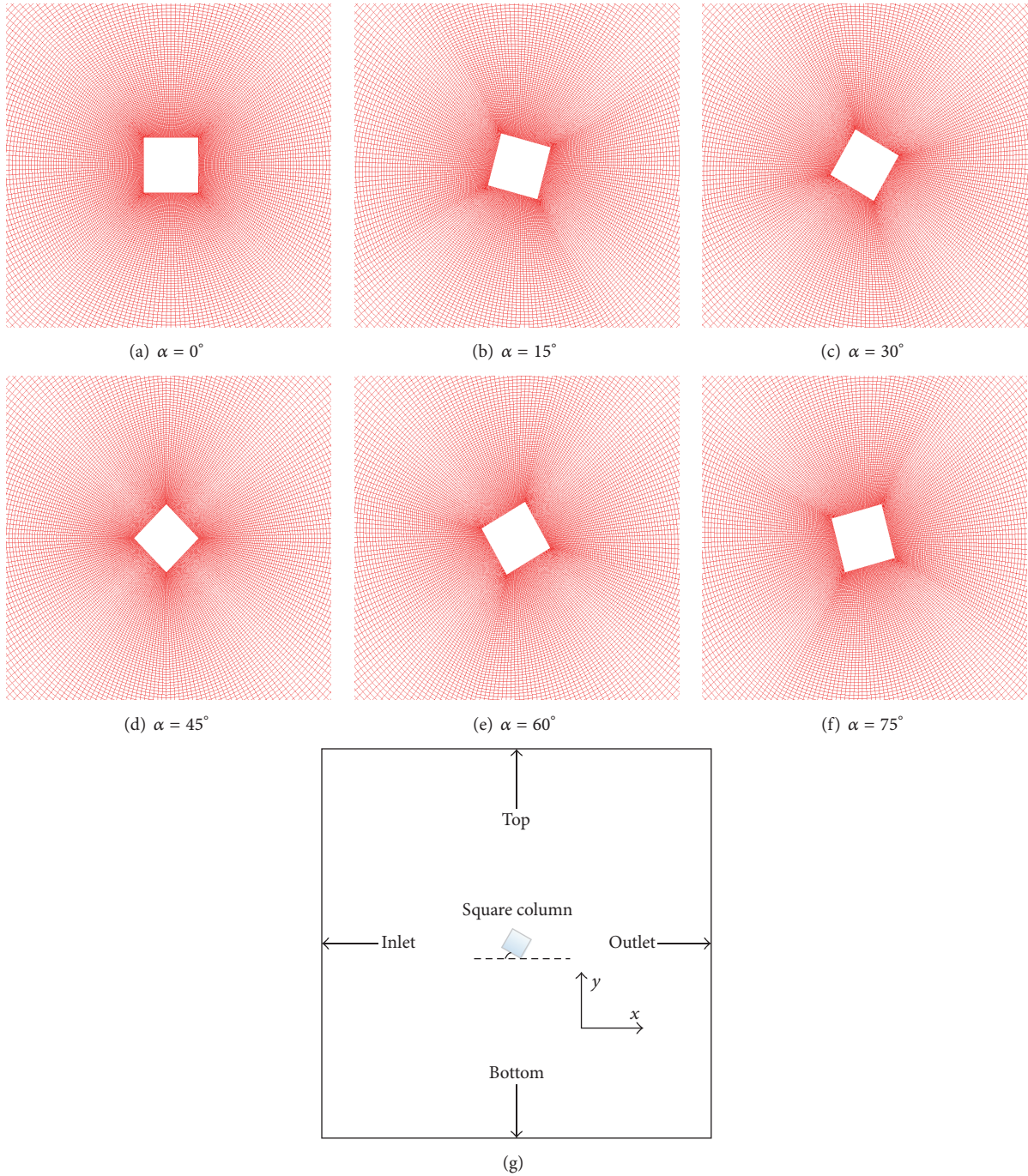


FIGURE 2: Computational grid and boundary conditions.

5.2. System Damping and Natural Frequency Characteristics.

The damping and natural frequency of the electromechanical coupling system can be obtained by MATLAB, and the real and imaginary parts of the circuit conjugate solutions are shown in Figure 3.

According to Figure 3, we can see that the total damping of the system is small when the resistance load is small. In the case of $R < 1 \times 10^5 \Omega$, the system total damping is increased with the resistance load increasing. Once the

resistance load R reaches $1 \times 10^5 \Omega$, the system total damping reaches the maximum value. It is noteworthy that the total damping of the system decreases instead of increasing when the resistance load keeps increasing; that is, $R > 1 \times 10^5 \Omega$. For the natural circular frequency, when $R < 3 \times 10^4 \Omega$, the frequency value remains at 44 rad/s; when $R > 2 \times 10^6 \Omega$, the frequency value approximately remains at 50 rad/s. Generally, the natural circular frequency value of the system is relatively stable, which is kept in the range of 44–50 rad/s.

TABLE 2: Run case of square column in OpenFOAM.

U (m/s)	U_{rsqu}			
	$\alpha = 0^\circ$	$\alpha = 15^\circ$ ($\alpha = 75^\circ$)	$\alpha = 30^\circ$ ($\alpha = 60^\circ$)	$\alpha = 45^\circ$
0.03927	3.5	2.85784	2.56223	2.47525
0.04488	4	3.26611	2.92826	2.82885
0.05049	4.5	3.67437	3.29429	3.18246
0.0561	5	4.08263	3.66032	3.53607
0.05834	5.2	4.24594	3.80673	3.67751
0.06059	5.4	4.40924	3.95315	3.81895
0.06283	5.6	4.57255	4.09956	3.9604
0.06732	6	4.89916	4.39239	4.24328
0.07293	6.5	5.30742	4.75842	4.59689
0.07854	7	5.71569	5.12445	4.9505
0.08415	7.5	6.12395	5.49048	5.3041
0.08976	8	6.53221	5.85652	5.65771
0.09537	8.5	6.94048	6.22255	6.01132

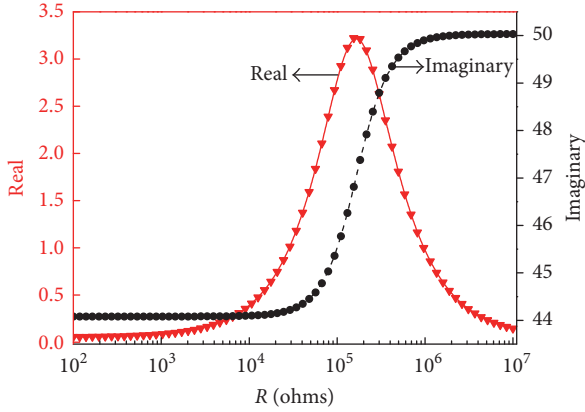


FIGURE 3: Real and imaginary parts of the circuit conjugate solutions.

5.3. *Vibration Characteristics of Square Column VIVPEH under Different Attack Angles.* In the following numerical simulations, we take the resistance load $R = 1 \times 10^6 \Omega$ and compute the amplitude response of the square column VIVPEH under different attack angles and different flow velocities, as shown in Figure 4. Note here that the natural frequency of square column is $f_n = 6.98 \text{ Hz}$, when the resistance load is $R = 1 \times 10^6 \Omega$. The dimensionless vibration amplitude Y_{squ}/D_{squ} is adopted to indicate the vibration response of the square column. The maximum value of Y_{squ} can be obtained by means of averaging the peak value of at least 60 displacement time-history response curves. In this paper, the vibration amplitude of the smooth circular column is provided to compare with that of the square column.

As we can see in Figure 4, different attack angles obviously have an effect on the peak vibration amplitude and lock-in region. Moreover, we can observe the “presynchronization,” “synchronization,” and “postsynchronization” of vortex-induced vibration curves of square column VIVPEH under different attack angles.

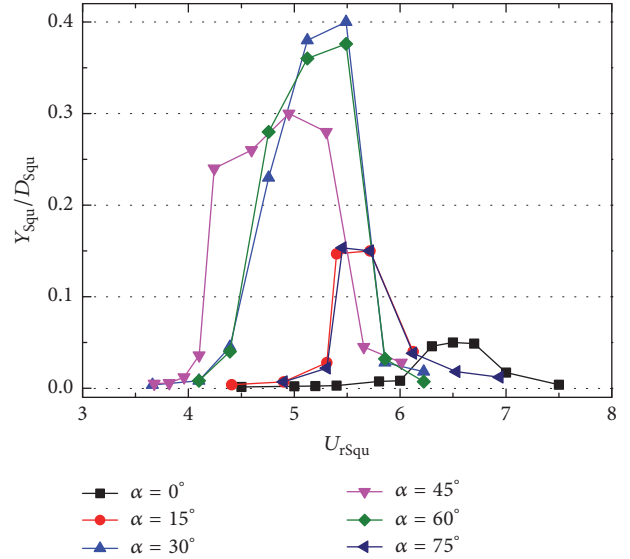


FIGURE 4: Dimensionless vibration amplitude of square column VIVPEH under different attack angles and different flow velocities.

5.3.1. $\alpha = 0^\circ$. The lock-in region is from $U_{rsqu} = 6.3$ to the end of $U_{rsqu} = 6.7$, and the maximum amplitude is $Y_{squamax}/D_{squ} = 0.05$, which appeared at $U_{rsqu} = 6.5$, as shown in Figure 4. In order to see more clearly about the vibration amplitude Y_{squ}/D_{squ} , some displacement time-history curves and FFT analysis results for $\alpha = 0^\circ$ are given in Figure 5. It can be seen that when U_{rsqu} is small, the amplitude of time-history curve presents a stable sinusoidal curve, and the maximum amplitude is so small that it can be ignored, which means that there is almost no vortex-induced vibration in the system. With the increases of U_{rsqu} , the system enters “presynchronization” phase and the vibration amplitude Y_{squ}/D_{squ} gradually increases. When the vortex shedding frequency approaches the natural frequency of square column VIVPEH, the oscillation amplitude of the square column VIVPEH

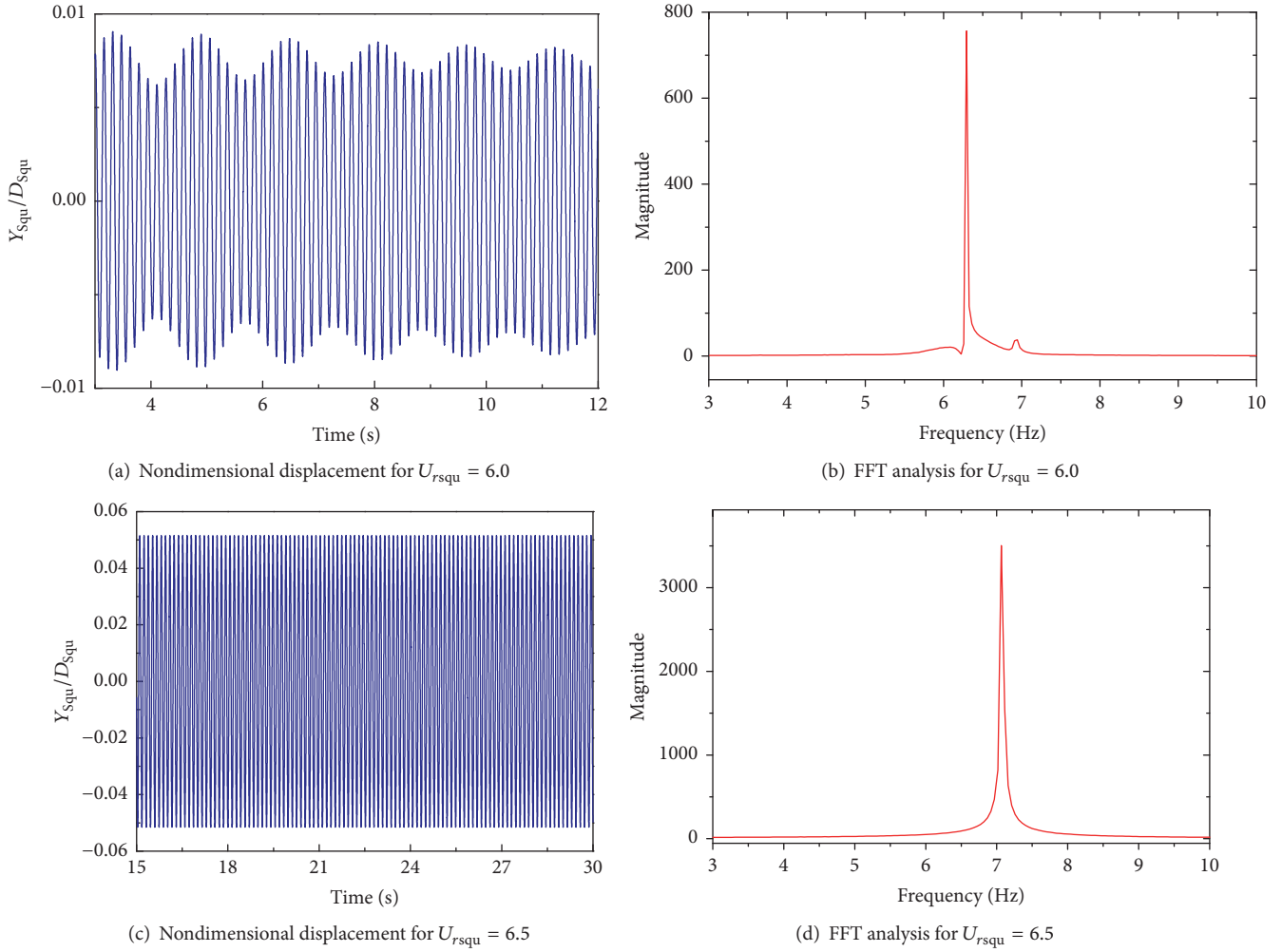


FIGURE 5: Displacement time-history and FFT analysis results for $\alpha = 0^\circ$.

increases significantly and the system enters synchronous phase, which means the phenomenon of “lock-in” occurs. Under synchronous phase, the vortex shedding frequency is kept constant and the amplitude of the system will remain at a higher value when the flow velocity U_{rsqu} is increased from $U_{rsqu} = 6.3$ to the end of $U_{rsqu} = 6.7$.

5.3.2. $\alpha = 15^\circ$. It can be seen from Figure 2(b) that there is a corner at the upper windward of the square column, which can obviously affect the flow field. As is shown in Figure 5, the maximum amplitude decreases and the lock-in region is narrow (from $U_{rsqu} = 5.4$ to $U_{rsqu} = 5.7$). The maximum amplitude is $Y_{squ\max}/D_{squ} = 0.148$, which appeared at $U_{rsqu} = 5.7$. The displacement time-history curves and FFT analysis results for $\alpha = 15^\circ$ are given in Figure 6. Similar with the results of $\alpha = 0^\circ$, the displacement time-history curve can also be divided into the following four stages: “unsynchronization,” “presynchronization,” “synchronization,” and “postsynchronization.”

5.3.3. $\alpha = 30^\circ$. The results in Figure 4 show that the maximum amplitude of the square column is obviously increased

with a wider range of lock-in region (from $U_{rsqu} = 4.5$ to $U_{rsqu} = 5.7$); the maximum amplitude $Y_{squ\max}/D_{squ}$ reaches 0.41. Similarly, some of the displacement time-history curves and FFT analysis results for $\alpha = 30^\circ$ are given in Figure 7. The results in Figure 7(a) show that the whole time-history curve appears as a parabolic shape and the growth rate decreased gradually to a stable level at late stage, which indicates the coupling of the vortex shedding frequency and natural frequency; that is, the lock-in phenomenon occurs. It can also be seen that there is a “beat” phenomenon in the amplitude curves, as shown in Figure 7(a). There are three peaks in the frequency spectrum curve, as shown in Figure 7(b), which indicates that three harmonics occur in the system. The explaining of the above phenomena is as follows. In the process of vortex-induced vibration of the square column, the vortex shedding frequency couples with the natural frequency when the flow velocity U_{rsqu} reaches a certain value. The flow field near the square column surface is strongly disturbed because of the corner point of the square column, which results in the superposition of three vibration frequencies. This is because the unbalance of the upper and lower aerodynamic force is caused by the obvious asymmetry

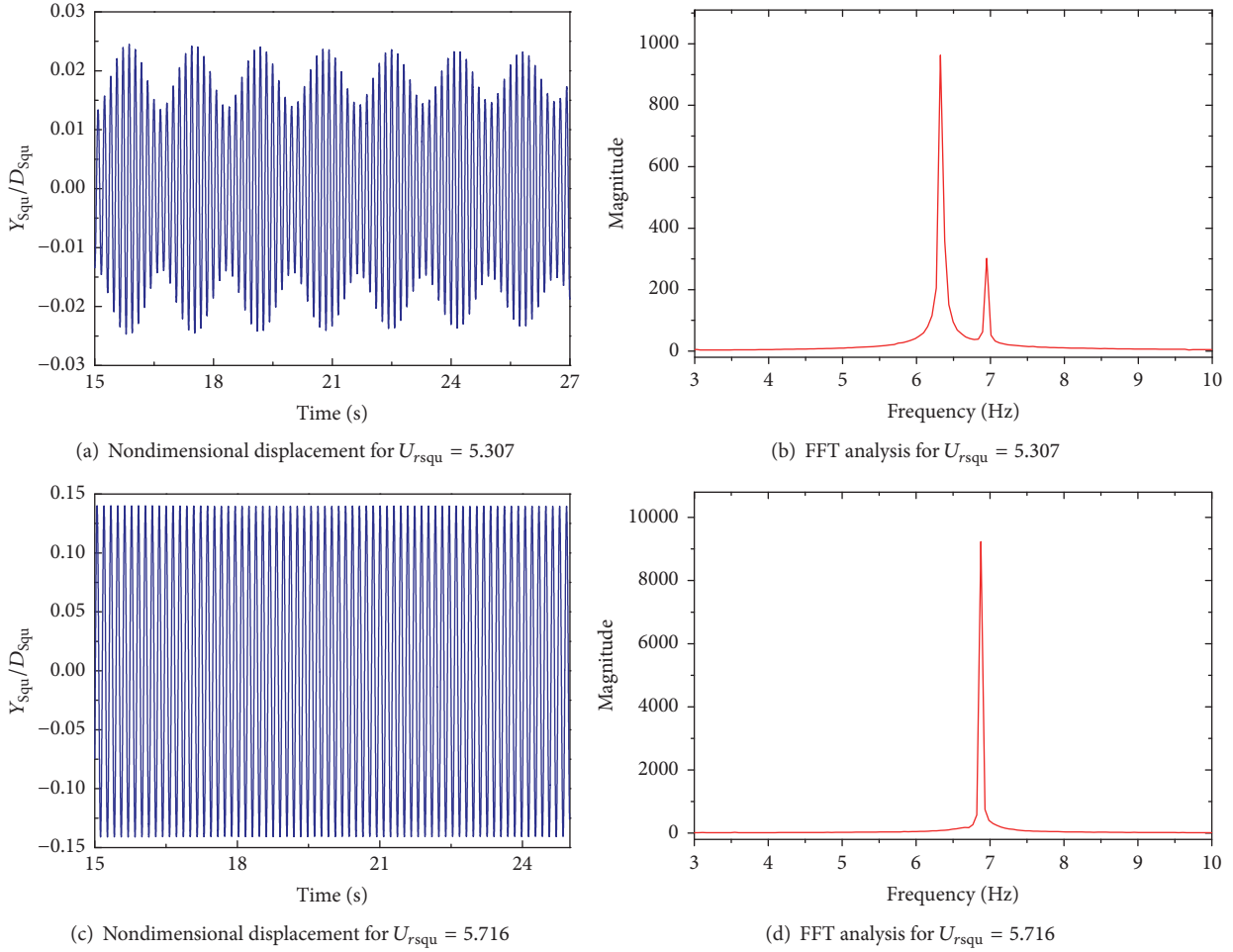


FIGURE 6: Displacement time-history and FFT analysis results for $\alpha = 15^\circ$.

under attack angle $\alpha = 30^\circ$. When the flow velocity is about $U_{rsqu} = 5.49$, as shown in Figures 7(c) and 7(d), the amplitude curve appears as a complete sine curve without noise. The maximum amplitude Y_{squmax}/D_{squ} is increased to about 0.41 and the vibration frequency is stabilized at 6.98 Hz, which can be regarded as the best working condition of square column VIVPEH.

5.3.4. $\alpha = 45^\circ$. As is shown in Figure 4, the displacement time-history curve can also be divided into the following four stages: “unsynchronization,” “presynchronization,” “synchronization,” and “postsynchronization.” The maximum amplitude is $Y_{squmax}/D_{squ} = 0.28$ and the lock-in region is from $U_{rsqu} = 4.2$ to the end of $U_{rsqu} = 5.4$, which appears earlier than that of other attack angles. The displacement time-history curves and FFT analysis results for $\alpha = 45^\circ$ are given in Figure 8. It can be seen that there is no severe aerodynamic disturbance, which shows that the vortex-induced vibration response of symmetric bluff body is relatively stable.

5.3.5. $\alpha = 60^\circ$. The displacement time-history curves and FFT analysis results for $\alpha = 60^\circ$ are given in Figure 9, which

are similar in shape to the one for $\alpha = 30^\circ$ with only slight differences in values. According to the displacement time-history curves, as shown in Figures 7 and 9, it can be seen that the amplitude results are almost exactly the same as the one for $\alpha = 30^\circ$ in the lock-in region. The same conclusion can also be obtained from the spectral analysis results; that is, the phenomena of harmonic and noise are similar. This is because the spring force of the system and the gravity of the column provide a balance in the flow field. So it can be considered that the above two cases of $\alpha = 30^\circ$ and $\alpha = 60^\circ$ are symmetric.

5.3.6. $\alpha = 75^\circ$. The results in Figure 10 show the displacement time-history curves and FFT analysis results for $\alpha = 75^\circ$. It is easy to see that both the displacement time-history curves and the spectral analysis results are similar to those of $\alpha = 15^\circ$ case, which indicates that the cases of $\alpha = 15^\circ$ and $\alpha = 75^\circ$ are also symmetric.

In order to verify the above conclusions, the *Strouhal Numbers* for the following four cases, $\alpha = 15^\circ$, $\alpha = 30^\circ$, $\alpha = 60^\circ$, and $\alpha = 75^\circ$, are compared with each other, as shown in Table 3. It can be seen that the *Strouhal Number* results for the case of $\alpha = 15^\circ$ ($\alpha = 30^\circ$) are almost equal to those for

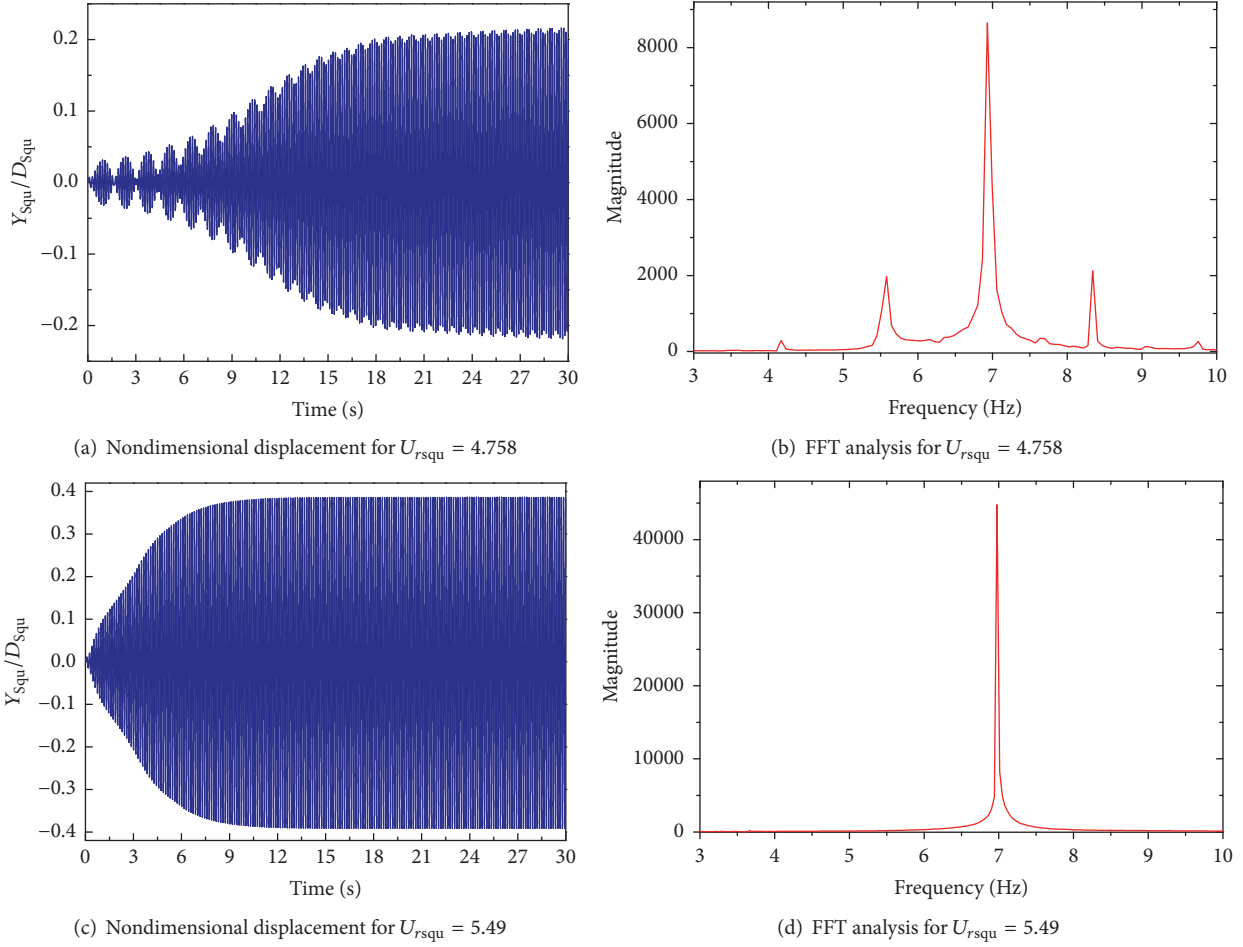


FIGURE 7: Displacement time-history and FFT analysis results for $\alpha = 30^\circ$.

TABLE 3: Comparison of *Strouhal Number* with different attack angle.

U (m/s)	Strouhal Number			
	15°	75°	30°	60°
0.05049	0.1682	0.1682	0.1832	0.1831
0.0561	0.1714	0.1714	0.1873	0.1872
0.06278	0.1743	0.1742	0.1896	0.1896
0.07293	0.1746	0.1746	0.1922	0.1922

the case of $\alpha = 75^\circ$ ($\alpha = 60^\circ$), which indicates that the above analysis is correct.

To show the difference more clearly of the lock-in region of square column VIVPEH under different attack angles, we choose the dimensionless frequency f_{squ}/f_{nsqu} to indicate the frequency characteristics of square column VIVPEH, where f_{squ} is the vortex shedding frequency of the system, which can be obtained by Fast Fourier Transform (FFT) of the displacement time-history curve, shown in Figures 5–10; f_{nsqu} is the natural frequency of the square column. The results in Figure 11 show the different lock-in regions of square column VIVPEH under different attack angles.

For the case of $\alpha = 0^\circ$, the range of values for the lock-in region is 6.5 to 7.0 ($6.5 \leq U_{rsqu} \leq 7.0$); the corresponding bandwidth value is 0.5. For the case of $\alpha = 15^\circ$ and $\alpha = 75^\circ$, the range of values for the lock-in region is 5.4 to 5.7 ($5.4 \leq U_{rsqu} \leq 5.7$); the corresponding bandwidth value is just 0.3. For the case of $\alpha = 30^\circ$ and $\alpha = 60^\circ$, the range of values for the lock-in region is 4.6 to 5.5 ($4.6 \leq U_{rsqu} \leq 5.5$), the corresponding bandwidth value is 0.9, which is significantly larger than that of the above two cases. When the attack angle is $\alpha = 45^\circ$, the range of values for the lock-in region is 4.2 to 5.4 ($4.2 \leq U_{rsqu} \leq 5.4$); the corresponding bandwidth value increases to 1.2. In addition, the three different branch types of square column VIVPEH can be observed in Figure 11, such as “presynchronization,” “synchronization,” and “postsynchronization.”

Based on the above analysis results, we believe that the calculation parameters and response parameters for the case of $\alpha = 15^\circ$ and $\alpha = 30^\circ$ are about the same as those for the case of $\alpha = 75^\circ$ and $\alpha = 60^\circ$.

5.4. Phase Angle Analysis of Square Column VIVPEH under Different Attack Angles. The analysis results of the initial phase angle and the synchronous phase angle of square

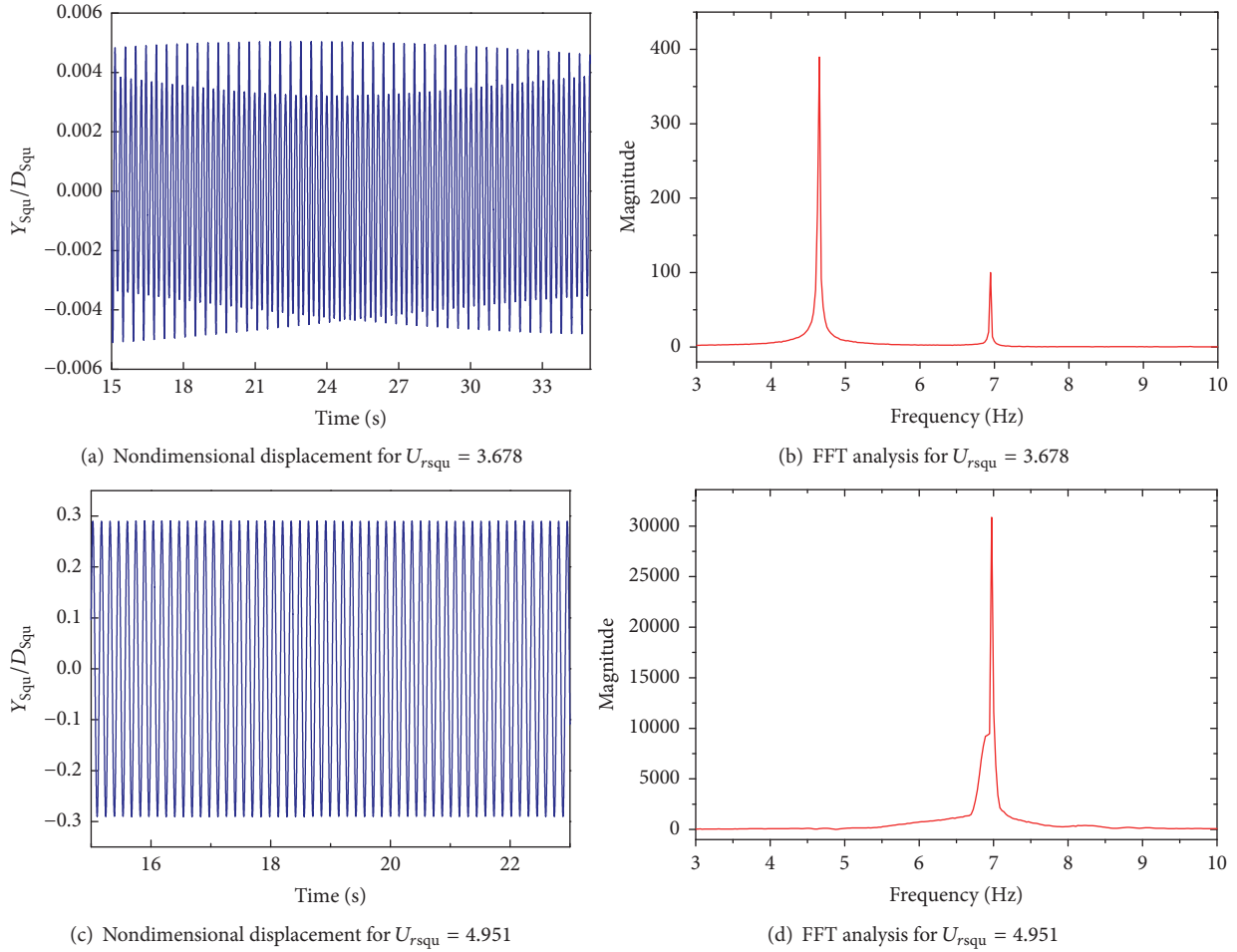


FIGURE 8: Displacement time-history and FFT analysis results for $\alpha = 45^\circ$.

column VIVPEH under different attack angles are given in Figures 12–15. It can be seen that the vibration is stable in the initial stage with a single amplitude and frequency, which is completely determined by the vortex shedding frequency. Therefore, the displacement time-history curve is almost synchronous with the lift coefficient curve without phase delay. This is because the amplitude is small, so that there is almost no stagnation when the vibration amplitude reaches its maximum or minimum value. Different from the initial vibration state, the vortex shedding frequency is locked again in the synchronous state, resulting in a multiple relationship between the vibration frequency and the natural frequency. That means, in synchronization region, there exists no phase difference between the vortex shedding frequency and vibration frequency. Accordingly, the displacement time-history curve is completely synchronized with the lift coefficient curve with some phase delay.

Figure 16 shows that the vortex-induced vibration of square column VIVPEH will stagnate for some time at the wave crest or the wave trough, because of the buffering effect of spring. As is shown in Figure 16(a), the vortices of V_1 and V_2 move forward to a distance of S_1 when the wave crests of the two adjacent steps appear. At the moment, V_1 obviously

becomes thinner and longer, while the vibration of the square column is still in the wave crest. Similarly, the vortices of V_3 and V_4 move forward to a distance of S_2 when the wave troughs of the two adjacent steps appear. It should be pointed out that, the vibration of the square column is always in the wave crest or the wave trough, which leads to the generation of the phase angle.

5.5. Analysis of Near Wake Vortex Shedding of Square Column VIVPEH under Different Attack Angles. The shapes of wake vortices in synchronized state of square column VIVPEH under different attack angles are given in Figures 17–20, in which T is the vibration period with subscript representing the value of an attack angle. The direction of the negative vorticity region is counterclockwise, which is expressed in blue; while the direction of the positive one is clockwise, which is expressed in red. It can be seen that, for the case of $\alpha = 0^\circ$, the flow field around the square column is stable, the vibration amplitude is small, and the wake vortex structure presents a regular 2S shape. In other words, a positive and negative vortex pair sheds in a cycle. For $\alpha = 15^\circ/\alpha = 75^\circ$, the position of near wake vortices shedding of square column VIVPEH began moving forward to the near column wall with

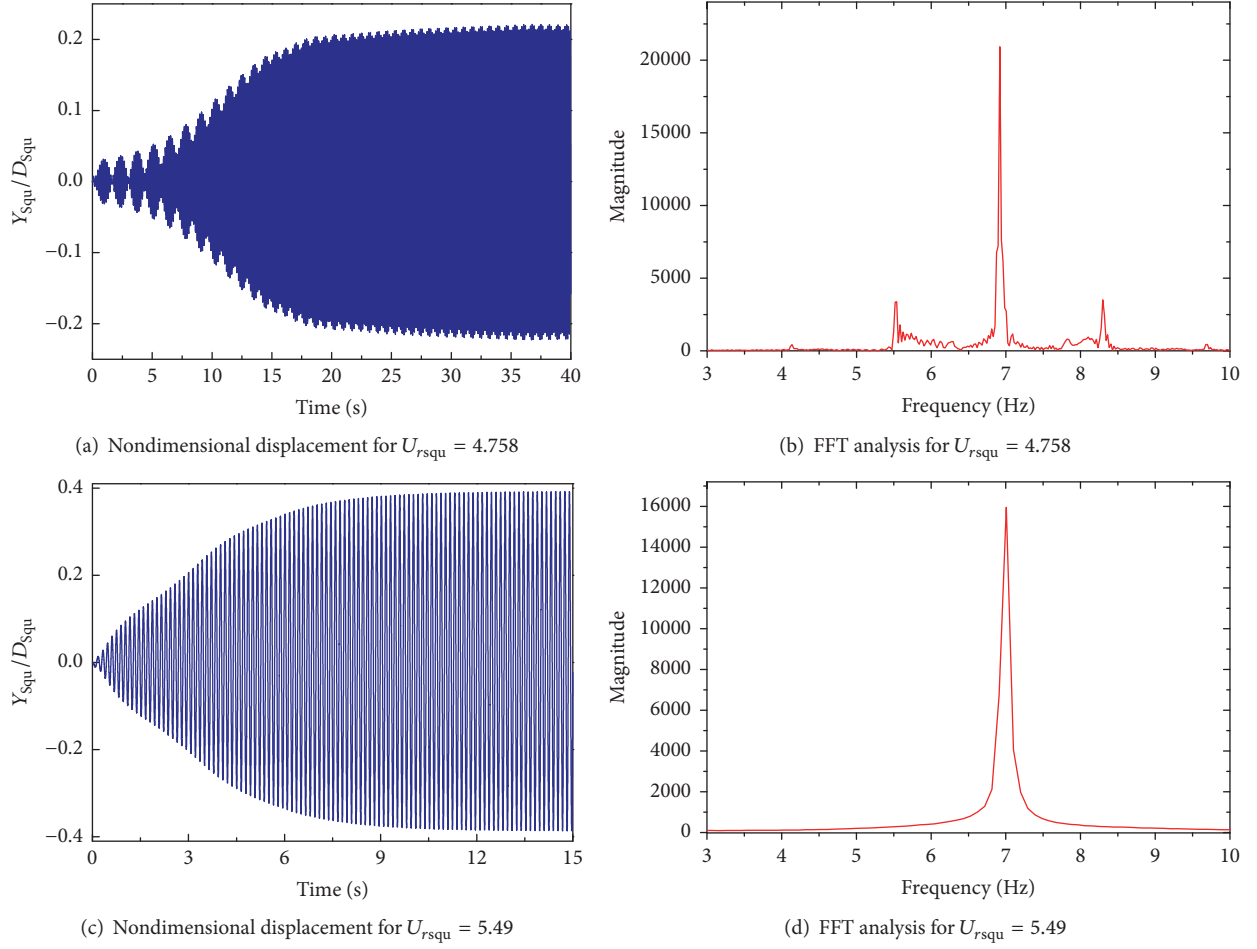


FIGURE 9: Displacement time-history and FFT analysis results for $\alpha = 60^\circ$.

increasing vibration amplitudes. Correspondingly, the wake vortex shedding array gradually changes its shape from 2S shape to a circle. As for $\alpha = 30^\circ/\alpha = 60^\circ$, it can be observed that the wake vortex shedding mode changes obviously with an increasing width of the vortex array, due to the increase of vibration amplitude and the shape of the vortex pair is changed from a flat shape to a regular elliptical shape. When the attack angle is $\alpha = 45^\circ$, the vibration amplitude decreases, which results in the wake vortex shedding mode changing back to the stable 2S mode.

5.6. Voltage Output and Power Output of Square Column VIVPEH under Different Attack Angles. Due to the influence of different attack angles, the vortex separation point of square column VIVPEH is different from that of cylinder, which results in the following analysis being more complicated. Considering the symmetric nature of the case $\alpha = 15^\circ/\alpha = 75^\circ$ and the case $\alpha = 30^\circ/\alpha = 60^\circ$, we take only the case of $\alpha = 0^\circ$, $\alpha = 15^\circ$, $\alpha = 30^\circ$, and $\alpha = 45^\circ$ in the following analysis of voltage output. When the resistance load is $R = 1 \times 10^6 \Omega$, the output voltage of the system can be calculated by (14).

The purpose of this section is to investigate the maximum value of the output voltage and the lock-in region to select the optimal attack angle of square column VIVPEH. The results of the maximum output voltage of square column VIVPEH under different attack angles and the effective working area of synchronization are given in Figure 21. It can be seen that the maximum output voltage of square column VIVPEH appears at the case of $\alpha = 45^\circ$ and the corresponding value is 6.732 V, while the minimum value appears at the case of $\alpha = 15^\circ/\alpha = 75^\circ$, which indicates that these two cases are not suitable for energy harvesting. Similarly, the output voltage of the case of $\alpha = 0^\circ$ is slightly higher than that of the case of $\alpha = 15^\circ/\alpha = 75^\circ$; however, its value is still small. When the attack angle increases from $\alpha = 15^\circ$ to $\alpha = 45^\circ$, the output voltage of square column VIVPEH system increases to its maximum value. The results of the working region of synchronization in Figure 21 show that the total bandwidth of the above six cases is (4.2–5.7, 5.3–5.7), and there are about 0.6 bandwidth of the region of nonsynchronization. The maximum bandwidth is (4.2–5.4) under attack angle $\alpha = 45^\circ$, which is higher than that of all other attack angle cases. Accordingly, the output power of the system can be calculated by (15).

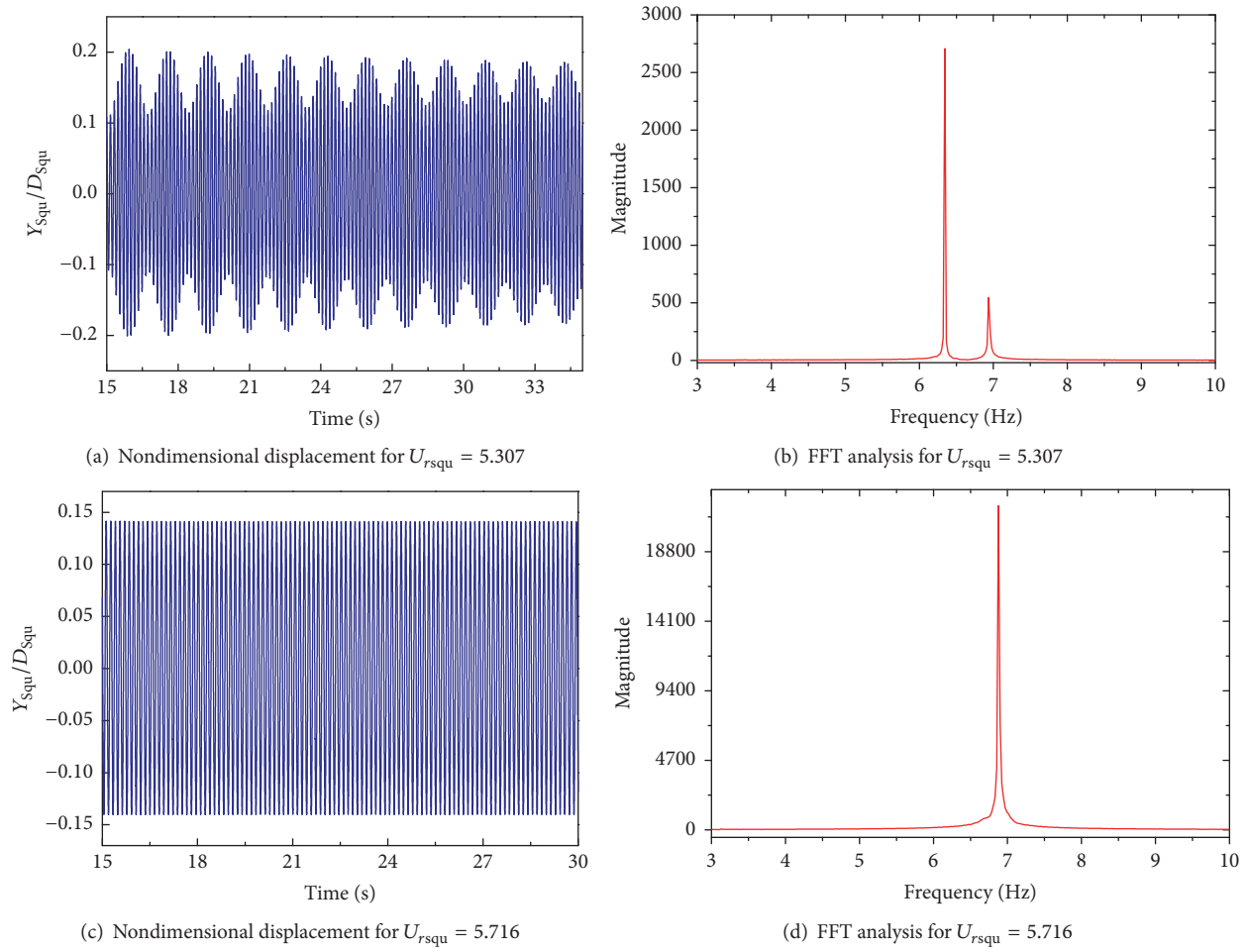


FIGURE 10: Displacement time-history and FFT analysis results for $\alpha = 75^\circ$.

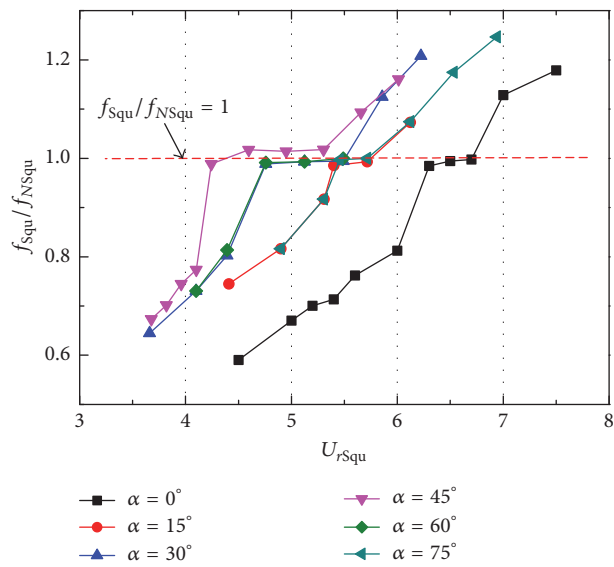


FIGURE 11: Nondimensional frequency of square column VIVPEH under different attack angles.

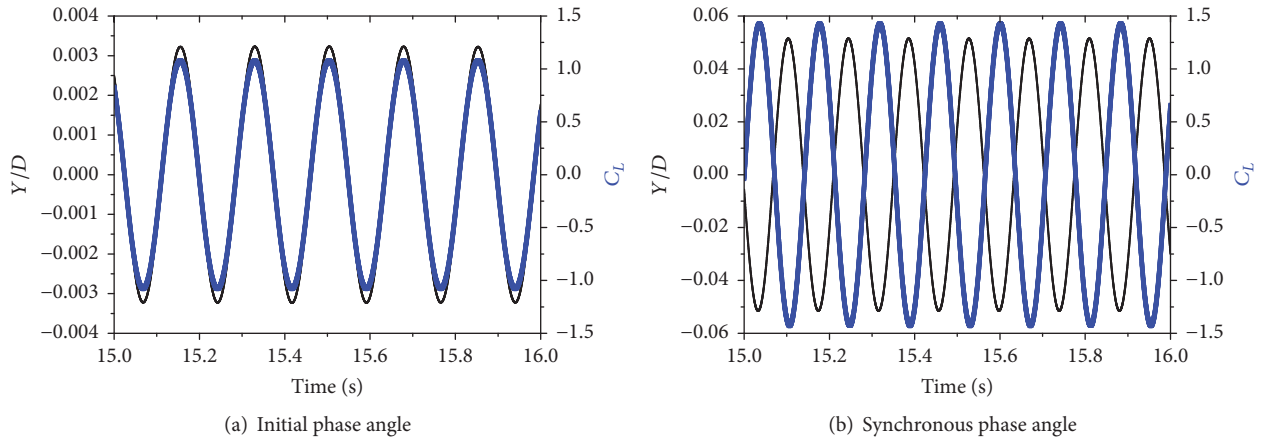


FIGURE 12: Results of phase angle in initial and synchronization state for $\alpha = 0^\circ$.

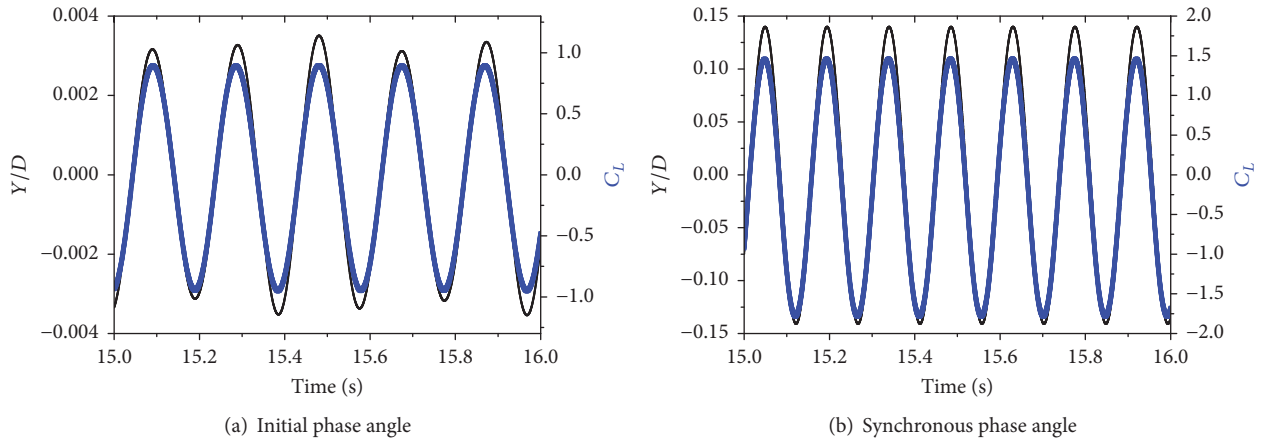


FIGURE 13: Results of phase angle in initial and synchronization state for $\alpha = 15^\circ / \alpha = 75^\circ$.

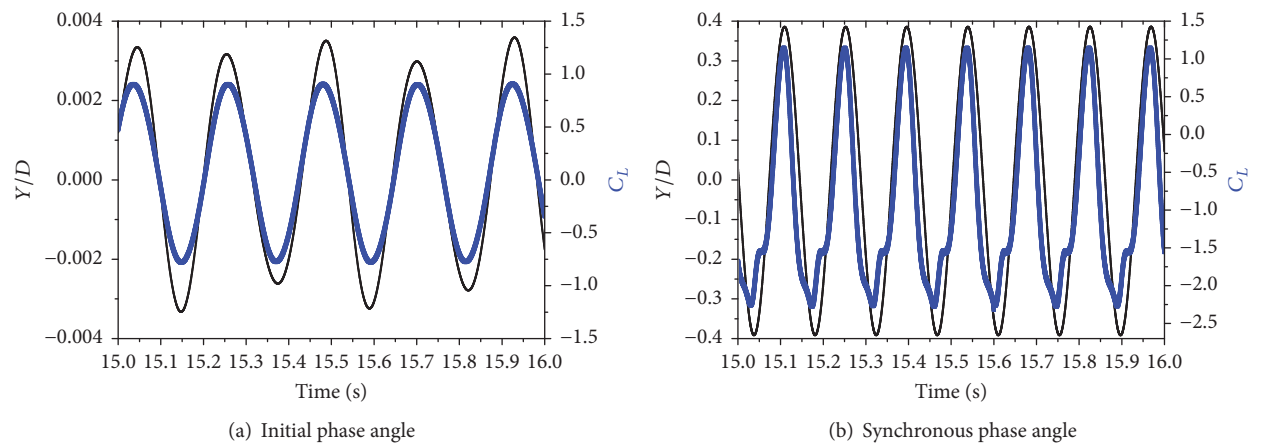


FIGURE 14: Results of phase angle in initial and synchronization state for $\alpha = 30^\circ / \alpha = 60^\circ$.

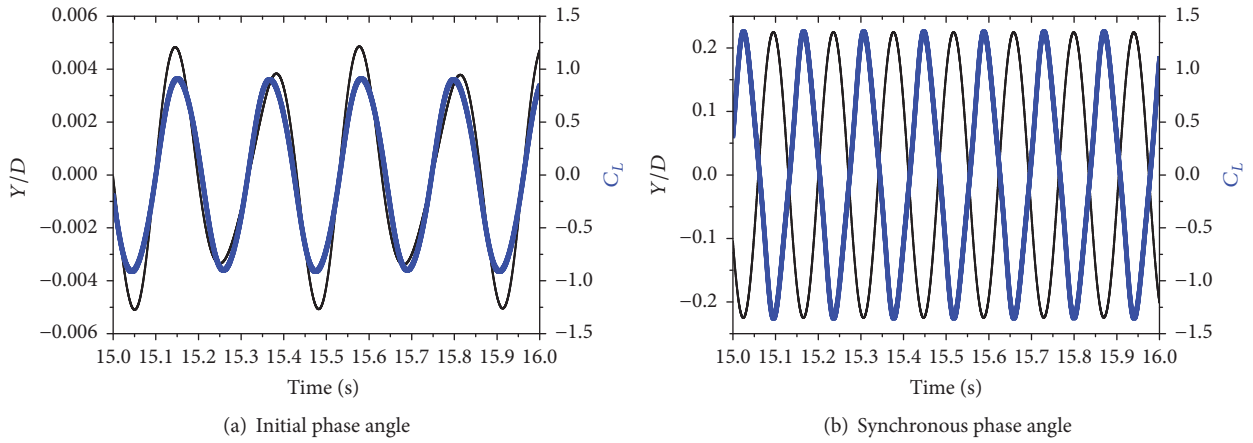


FIGURE 15: Results of phase angle in initial and synchronization state for $\alpha = 45^\circ$.

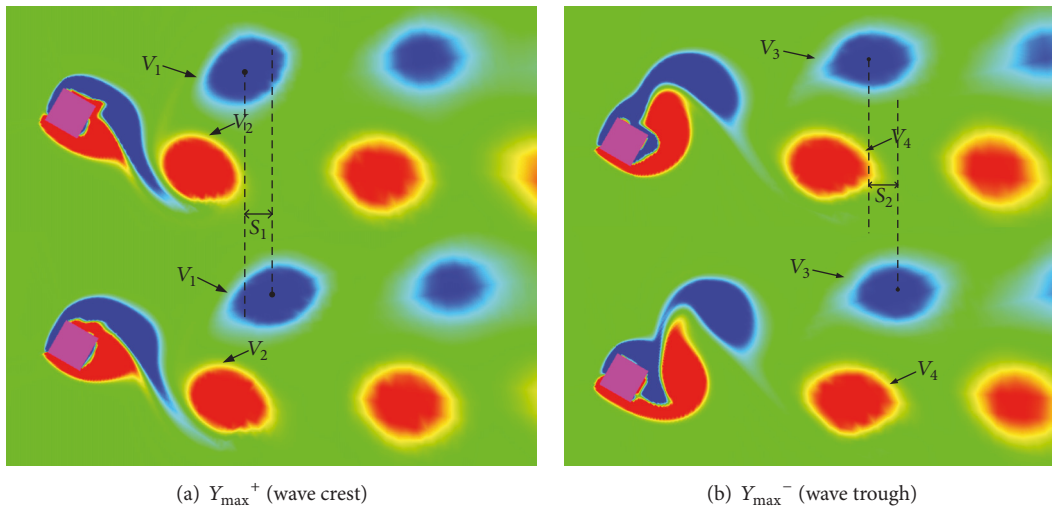


FIGURE 16: Diagram of phase angle between displacement and lift force development history.

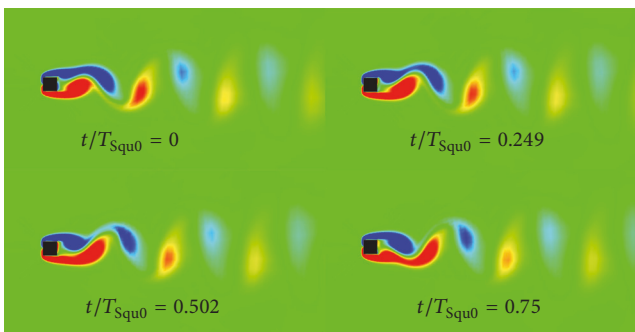


FIGURE 17: Vortex structures in synchronization region for $\alpha = 0^\circ$.

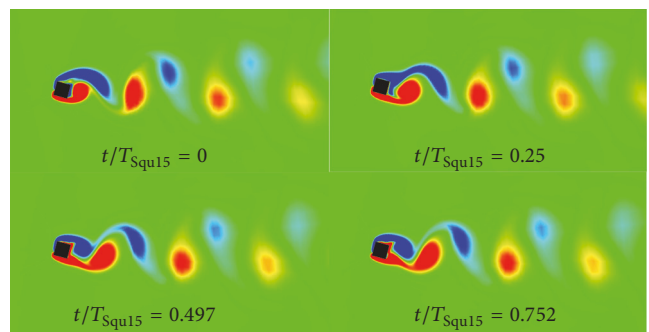


FIGURE 18: Vortex structures in synchronization region for $\alpha = 15^\circ/\alpha = 75^\circ$.

The results of the maximum output power of square column VIVPEH under different attack angles are given in Figure 22. It can also be seen that the maximum value of the output power appears at the case of $\alpha = 45^\circ$ and

the corresponding value is 4.5×10^{-5} W. Therefore, square column VIVPEH under attack angle $\alpha = 45^\circ$ is an ideal PEH, because of its higher voltage output value and larger working bandwidth.

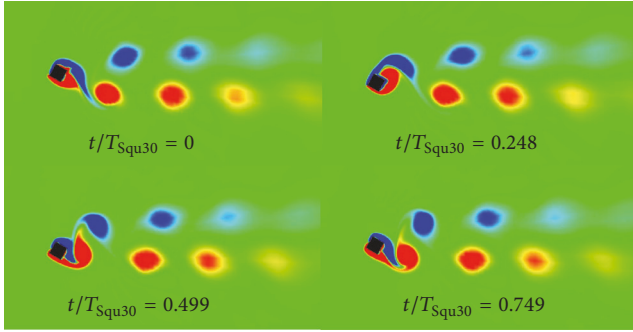


FIGURE 19: Vortex structures in synchronization region for $\alpha = 30^\circ/\alpha = 60^\circ$.

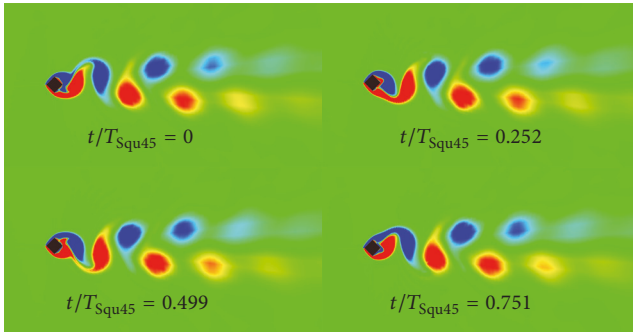


FIGURE 20: Vortex structures in synchronization region for $\alpha = 45^\circ$.

6. Conclusions

The energy harvesting features of square column VIVPEH under different attack angles are investigated in this paper with considering the vibration characteristics, phase characteristics, the near wake vortex shedding mode, and the output voltage and power of the system. The main conclusions are as follows:

- (1) Within the range of reduced velocity studied in this paper, the vortex-induced vibration curves of square column VIVPEH under different attack angles can be obtained, which contains the phenomena of “presynchronization,” “synchronization,” and “postsynchronization.” The vortex shedding shape of square column VIVPEH is dominated by 2S mode.
- (2) The attack angle has significant effect on the maximum value of vibration amplitude of square column and the lock-in region. Due to the influence of different attack angles, the boundary layer separation point does not move backwards like the cylinder. The maximum vibration amplitude and the lock-in vibration region of square column will also fluctuate. When the attack angle is equal to 45 degrees, the synchronization region can reach a value of 1.2 times of reduction velocity.
- (3) The numerical analysis shows that the cases of $\alpha = 15^\circ/\alpha = 30^\circ$ and $\alpha = 75^\circ/\alpha = 60^\circ$ for square column VIVPEH are symmetric, which indicates that

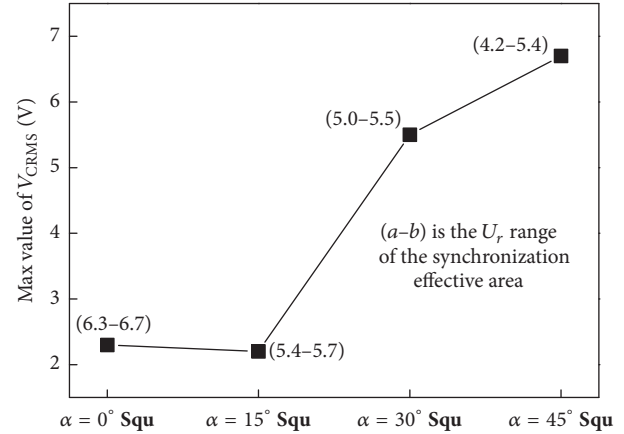


FIGURE 21: Comparison of maximum value of voltage output and synchronization effective area between VIVPEH with different shapes.

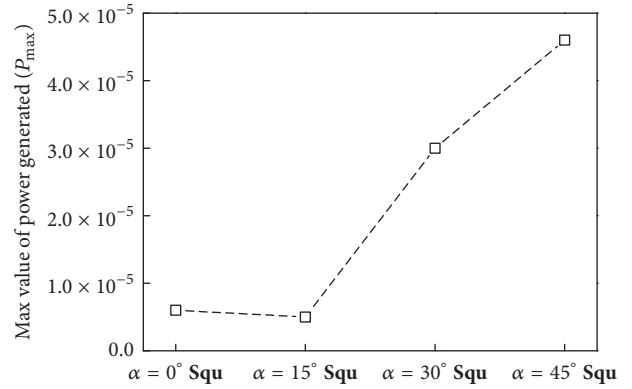


FIGURE 22: Comparison of maximum value of power output between VIVPEH with different shapes.

the calculated results of the case of $\alpha = 15^\circ/\alpha = 30^\circ$ are equal to the results of case of $\alpha = 75^\circ/\alpha = 60^\circ$, respectively.

- (4) The maximum value of the output power is similar to that of the output voltage, which appears at the case of $\alpha = 45^\circ$ and the corresponding value is 4.5×10^{-5} W and 6.732 V, respectively. Therefore, $\alpha = 45^\circ$ is a relatively ideal attack angle of square column VIVPEH.

Conflicts of Interest

The authors declare that there are no conflicts of interest regarding the publication of this paper.

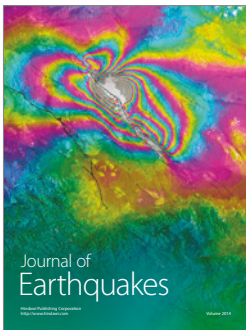
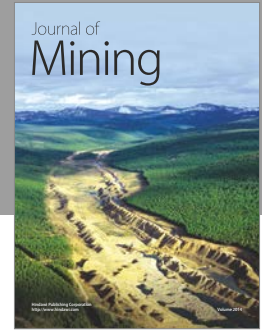
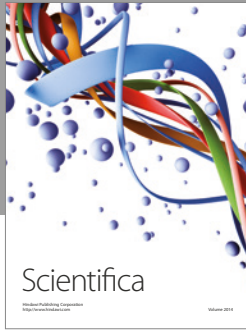
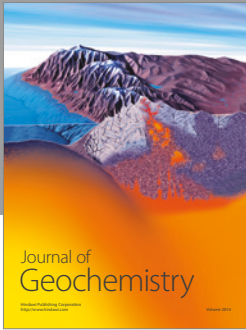
Acknowledgments

This research has been funded by the National Natural Science Foundation of China (Grants nos. 51606171, 51578512, and 51108425) and the Outstanding Young Talent Research Fund of Zhengzhou University (Grant no. 1521322004).

References

- [1] K. A. Cook-Chennault, N. Thambi, and A. M. Sastry, "Powering MEMS portable devices—a review of non-regenerative and regenerative power supply systems with special emphasis on piezoelectric energy harvesting systems," *Smart Materials and Structures*, vol. 17, no. 4, pp. 1240–1246, 2008.
- [2] J. A. Paradiso and T. Starner, "Energy scavenging for mobile and wireless electronics," *IEEE Pervasive Computing*, vol. 4, no. 1, pp. 18–27, 2005.
- [3] N. S. Shenck and J. A. Paradiso, "Energy scavenging with shoe-mounted piezoelectrics," *IEEE Micro*, vol. 21, no. 3, pp. 30–42, 2001.
- [4] G. K. Ottman, H. F. Hofmann, A. C. Bhatt, and G. A. Lesieutre, "Adaptive piezoelectric energy harvesting circuit for wireless remote power supply," *IEEE Transactions on Power Electronics*, vol. 17, no. 5, pp. 669–676, 2002.
- [5] S. P. Beeby, M. J. Tudor, and N. M. White, "Energy harvesting vibration sources for microsystems applications," *Measurement Science and Technology*, vol. 17, no. 12, pp. R175–R195, 2006.
- [6] S. Roundy, P. K. Wright, and J. Rabaey, "A study of low level vibrations as a power source for wireless sensor nodes," *Computer Communications*, vol. 26, no. 11, pp. 1131–1144, 2003.
- [7] J. Wang, J. Ran, and Z. Zhang, "Energy harvester based on the synchronization phenomenon of a circular cylinder," *Mathematical Problems in Engineering*, vol. 2014, Article ID 567357, 9 pages, 2014.
- [8] J. Wang, S. Wen, X. Zhao, M. Zhang, and J. Ran, "Piezoelectric Wind Energy Harvesting from Self-Excited Vibration of Square Cylinder," *Journal of Sensors*, vol. 2016, Article ID 2353517, 12 pages, 2016.
- [9] M. Zhang and J. Wang, "Experimental study on piezoelectric energy harvesting from vortex-induced vibrations and wake-induced vibrations," *Journal of Sensors*, vol. 2016, Article ID 2673292, 7 pages, 2016.
- [10] C. H. K. Williamson, "Vortex dynamics in the cylinder wake," *Annual Review of Fluid Mechanics*, vol. 28, pp. 477–539, 1996.
- [11] C. H. Williamson and R. Govardhan, "Vortex-induced vibrations," *Annual Review of Fluid Mechanics*, vol. 36, no. 1, pp. 413–455, 2004.
- [12] J. J. Allen and A. J. Smits, "Energy harvesting eel," *Journal of Fluids and Structures*, vol. 15, no. s3-s4, pp. 629–640, 2001.
- [13] G. W. Taylor, J. R. Burns, S. M. Kammann, W. B. Powers, and T. R. Welsh, "The energy harvesting Eel: a small subsurface ocean/river power generator," *IEEE Journal of Oceanic Engineering*, vol. 26, no. 4, pp. 539–547, 2001.
- [14] M. M. Bernitsas, K. Raghavan, Y. Ben-Simon, and E. M. H. Garcia, "VIVACE (vortex induced vibration aquatic clean energy): a new concept in generation of clean and renewable energy from fluid flow," *Journal of Offshore Mechanics and Arctic Engineering*, vol. 130, no. 4, Article ID 041101, 15 pages, 2008.
- [15] M. M. Bernitsas, Y. Ben-Simon, K. Raghavan, and E. M. H. Garcia, "The VIVACE converter: model tests at high damping and reynolds number around 10^5 ," *Journal of Offshore Mechanics and Arctic Engineering*, vol. 131, no. 1, pp. 1–12, 2009.
- [16] J. H. Lee, N. Xiros, and M. M. Bernitsas, "Virtual damper-spring system for VIV experiments and hydrokinetic energy conversion," *Ocean Engineering*, vol. 38, no. 16, pp. 732–747, 2011.
- [17] J. H. Lee and M. M. Bernitsas, "High-damping, high-Reynolds VIV tests for energy harnessing using the VIVACE converter," *Ocean Engineering*, vol. 38, no. 16, pp. 1697–1712, 2011.
- [18] K. Raghavan and M. M. Bernitsas, "Experimental investigation of Reynolds number effect on vortex induced vibration of rigid circular cylinder on elastic supports," *Ocean Engineering*, vol. 38, no. 5-6, pp. 719–731, 2011.
- [19] K. Raghavan and M. M. Bernitsas, "Enhancement of high damping VIV through roughness distribution for energy harnessing at $8 \times 10^3 < Re < 1.5 \times 10^5$," in *Proceedings of the 27th International Conference on Offshore Mechanics and Arctic Engineering, OMAE '08*, pp. 871–882, June 2008.
- [20] C.-C. Chang, R. Ajith Kumar, and M. M. Bernitsas, "VIV and galloping of single circular cylinder with surface roughness at $3.0 \times 10^4 \leq Re \leq 1.2 \times 10^5$," *Ocean Engineering*, vol. 38, no. 16, pp. 1713–1732, 2011.
- [21] W. Wu, M. M. Bernitsas, and K. Maki, "Simulation vs. experiments of flow induced motion of circular cylinder with passive turbulence control at $35,000 \leq Re \leq 130,000$," in *Proceedings of the ASME 2011 30th International Conference on Ocean, Offshore and Arctic Engineering*, vol. 136, pp. 548–557, American Society of Mechanical Engineers, Rotterdam, Netherlands, June 2011.
- [22] L. Ding, M. M. Bernitsas, and E. S. Kim, "2-D URANS vs. experiments of flow induced motions of two circular cylinders in tandem with passive turbulence control for $30,000 \leq Re \leq 105,000$," *Ocean Engineering*, vol. 72, pp. 429–440, 2013.
- [23] A. Abdelkefi, M. R. Hajj, and A. H. Nayfeh, "Phenomena and modeling of piezoelectric energy harvesting from freely oscillating cylinders," *Nonlinear Dynamics. An International Journal of Nonlinear Dynamics and Chaos in Engineering Systems*, vol. 70, no. 2, pp. 1377–1388, 2012.
- [24] A. Abdelkefi, A. H. Nayfeh, and M. R. Hajj, "Modeling and analysis of piezoaeroelastic energy harvesters," *Nonlinear Dynamics. An International Journal of Nonlinear Dynamics and Chaos in Engineering Systems*, vol. 67, no. 2, pp. 925–939, 2012.
- [25] A. Mehmood, A. Abdelkefi, M. R. Hajj, A. H. Nayfeh, I. Akhtar, and A. O. Nuhait, "Piezoelectric energy harvesting from vortex-induced vibrations of circular cylinder," *Journal of Sound and Vibration*, vol. 332, no. 19, pp. 4656–4667, 2013.
- [26] A. Abdelkefi and A. O. Nuhait, "Modeling and performance analysis of cambered wing-based piezoaeroelastic energy harvesters," *Smart Materials and Structures*, vol. 22, no. 9, Article ID 095029, 2013.
- [27] H. L. Dai, A. Abdelkefi, and L. Wang, "Piezoelectric energy harvesting from concurrent vortex-induced vibrations and base excitations," *Nonlinear Dynamics*, vol. 77, no. 3, pp. 967–981, 2014.
- [28] Z. Yan and A. Abdelkefi, "Nonlinear characterization of concurrent energy harvesting from galloping and base excitations," *Nonlinear Dynamics*, vol. 77, no. 4, pp. 1171–1189, 2014.
- [29] W. P. Robbins, I. Marusic, D. Morris et al., "Wind-generated electrical energy using flexible piezoelectric materials," in *Proceedings of the ASME 2006 International Mechanical Engineering Congress and Exposition American Society of Mechanical Engineers*, vol. 23, pp. 581–590, 2006.
- [30] H. D. Akaydin, N. Elvin, and Y. Andreopoulos, "Wake of a cylinder: a paradigm for energy harvesting with piezoelectric materials," *Experiments in Fluids*, vol. 49, no. 1, pp. 291–304, 2010.
- [31] X. Gao, W.-H. Shih, and W. Y. Shih, "Flow energy harvesting using piezoelectric cantilevers with cylindrical extension," *IEEE Transactions on Industrial Electronics*, vol. 60, no. 3, pp. 1116–1118, 2013.

- [32] H. D. Akaydin, N. Elvin, and Y. Andreopoulos, “The performance of a self-excited fluidic energy harvester,” *Smart Materials Structures*, vol. 21, no. 2, Article ID 025007, 2012.
- [33] P. R. Spalart and S. R. Allmaras, “A one-equation turbulence model for aerodynamic flows,” *La Recherche Aéronautique*, vol. 439, no. 1, pp. 5–21, 2003.
- [34] A. Barrero-Gil, A. Sanz-Andrés, and G. Alonso, “Hysteresis in transverse galloping: the role of the inflection points,” *Journal of Fluids and Structures*, vol. 25, no. 6, pp. 1007–1020, 2009.



Hindawi

Submit your manuscripts at
<https://www.hindawi.com>

